ELSEVIER

NeuroImage

www.elsevier.com/locate/ynimg
NeuroImage 26 (2005) 1042 – 1051

Mapping postnatal mouse brain development with diffusion tensor microimaging

Jiangyang Zhang,[a,b] Michael I. Miller,[b,c] Celine Plachez,[d] Linda J. Richards,[d] Paul Yarowsky,[e] Peter van Zijl,[a,f] and Susumu Mori[a,f,*]

[a]*Johns Hopkins University, School of Medicine, Department of Radiology, Division of NMR Research, 720 Rutland Avenue, Baltimore, MD 21205, USA*
[b]*Department of Biomedical Engineering, 720 Rutland Avenue, Baltimore, MD 21205, USA*
[c]*Johns Hopkins University, Center of Imaging Science, 3400 North Charles Street, Baltimore, MD 21218, USA*
[d]*University of Maryland School of Medicine, Department of Anatomy and Neurobiology and The Program in Neuroscience, 685 West Baltimore Street, Baltimore, MD 21201, USA*
[e]*Department of Pharmacology and Experimental Therapeutics, 685 West Baltimore Street, Baltimore, MD 21201, USA*
[f]*F.M. Kirby Research Center for Functional Brain Imaging, Kennedy Krieger Institute, 707 North Broadway, Baltimore, MD 21205, USA*

Received 27 August 2004; revised 26 February 2005; accepted 10 March 2005
Available online 21 April 2005

While mouse brain development has been extensively studied using histology, quantitative characterization of morphological changes is still a challenging task. This paper presents how developing brain structures can be quantitatively characterized with magnetic resonance diffusion tensor microimaging coupled with techniques of computational anatomy. High resolution diffusion tensor images of ex vivo postnatal mouse brains provide excellent contrasts to reveal the evolutions of mouse forebrain structures. Using anatomical landmarks defined on diffusion tensor images, tissue level growth patterns of mouse brains were quantified. The results demonstrate the use of these techniques to three-dimensionally and quantitatively characterize brain growth.

Keywords: Mouse brain development; Diffusion tensor; Microimaging; Computational neuroanatomy

Introduction

In recent years, the number of studies on brain development using laboratory mice has increased enormously due to advances in gene engineering technologies and the increasing availability of various mutant mouse strains. These studies add to the information on the molecular and cellular mechanisms of mouse brain development. There are a number of sources describing embryonic mouse brain morphogenesis (Alvarez-Bolado and Swanson, 1996; Bayer and Altman, 1991; Bayer et al., 1994; Paxinos et al., 1994) and adult mouse brain anatomy (Paxinos and Franklin, 2000). However, quantitative three-dimensional information on the development of mouse brain morphology is still scarce.

Most studies on brain development have relied on histological examination, in which rich cellular and/or molecular information can be obtained with high spatial resolution. However, histological examination is not optimal for three-dimensional macroscopic characterization of anatomical changes because it requires large amounts of sectioned slides. Sectioning procedures can easily lead to complications such as tissue damage, deformation, and section-to-section variation. Consequently, histology-based studies are often confined to small areas and are hypothesis-driven or based on a priori knowledge so that optimum slice locations and staining methods can be designed. While histology-based studies remain the most valuable tool for neuroanatomical examination, methods of 3D imaging should greatly enhance our ability for phenotype characterization by providing accurate and efficient means for morphological delineation.

Several alternative techniques, including magnetic resonance imaging (MRI) (Jacobs and Fraser, 1994; Jacobs et al., 1999a,b; Johnson et al., 1993, 2002) and optical methods (Sharpe et al., 2002; Weninger and Mohun, 2002), have been developed and have shown great potential. Among them, three-dimensional MRI has the capability of delineating anatomical structures inside optically opaque samples with the potential of in vivo longitudinal studies. Although it has been successfully used in several developmental studies (Baratti et al., 1999; Jacobs and Fraser, 1994; Jacobs et al., 1999a,b; Mori et al., 2001), conventional relaxation-based MRI often fails to provide satisfactory tissue contrast for mouse brains at embryonic or paranatal stages, mostly due to lack of myelination.

Recently, we and other groups demonstrated that diffusion tensor imaging (DTI) can delineate detailed neuroanatomy of developing

* Corresponding author. Department of Radiology, Johns Hopkins University School of Medicine, 217 Traylor Building, 720 Rutland Avenue, Baltimore, MD 21205, USA.
E-mail address: susumu@mri.jhu.edu (S. Mori).
Available online on ScienceDirect (www.sciencedirect.com).

1053-8119/$ - see front matter © 2005 Elsevier Inc. All rights reserved.
doi:10.1016/j.neuroimage.2005.03.009

mouse brains with endogenous tissue contrast that has not been accessible by any other non-invasive, 3D imaging modalities (Mori et al., 2001; Zhang et al., 2003). This technique provides us an exciting new opportunity to accurately and quantitatively characterize 3D growth pattern of various brain structures.

With the availability of three-dimensional mouse brain images, quantitative measurement of evolving neuroanatomy becomes the next logical step. Following the early envisage of D'Arcy Thompson on using transformations to study biological forms, techniques of computational anatomy (CA) (Grenander and Miller, 1998; Miller et al., 1997, 2002; Toga and Thompson, 2003; van Pelt et al., 2001) are emerging for the quantitative metric study of growth and aging (Thompson et al., 2000, 2001a,b, 2003). Several groups have developed methodologies for the comparison of geometric structures based on maps on the dense continuum connecting anatomical configurations to extrinsic atlases (Bookstein, 1996; Chung et al., 2001; Dann et al., 1989; Evans et al., 1996; Good et al., 2001; Thompson et al., 2001a,b). The sheer complexity of brain anatomy requires the study of all submanifolds—landmarks, curves, surfaces, and subvolumes, all taken together forming the complete volume (Christensen et al., 1996; Miller and Younes, 2001; Miller et al., 1997). Using conventional MRI, we have been able to map the shape and structures of midbrain including the hippocampus and thalamus using diffeomorphisms generated via the differential equations of particle flows, in particular large deformation diffeomorphic metric mapping (LDDMM) (Beg et al., 2003; Miller et al., 2002). The transformations constructed by the LDDMM methods are diffeomorphisms so that connected structures remain connected, disjoint structures remain disjoint and submanifolds are preserved.

In this paper, we first investigated contrast change in DTI and conventional MR images throughout development. Identifiable structures were then manually segmented and their volume changes were observed. Morphometric changes of the neocortex due to growth were analyzed based on manual landmark placement followed by LDDMM. These results could quantitatively delineate normal developmental processes of male C57/BL mouse brains. This approach provides an important foundation for future applications to study of brain developmental abnormalities due to gene alteration (phenotype), induced lesions (e.g., ischemic or viral insults) or drug treatment (e.g., maternal drug addiction), by filling the gap between cellular/molecular changes and gross anatomical observation, and further our understanding of the underlying mechanisms involved.

Methods

Animal subjects

All experiments and procedures were approved by the Animal Research Committee of the Johns Hopkins University, School of Medicine. We used C57BL/6J male mice as the subject of our study. A total of 25 mice were used in this study, ranging from embryonic day 18 (E18) to postnatal day 80 (P80). Among them, 3 mice were at P0 and 16 mice were at P7, P20, P30 and P80 (4 mice at each stage). Specimens were fixed with 4% paraformaldehyde in phosphate-buffered saline (PBS) for over 1 month. Before imaging, we placed specimens in PBS for more than 24 h to washout the fixation solution and transferred them into home-built MR-compatible tubes. The tubes were then filled with fomblin (Fomblin Profludropolyether, Ausimont, Thorofare, New Jersey, USA) to prevent dehydration.

Image acquisition and processing

Imaging was performed using a GE Omega 400 (9.4T) spectrometer. Custom-made solenoid volume coils were used as both the radio frequency (RF) signal transmitter and receiver. The NMR sequence was based on a 3D multiple echo sequence with navigator-echo phase correction scheme and segmented k-space acquisition (Mori and van Zijl, 1998). Following each excitation, two imaging echoes were acquired followed by two navigator echoes to correct any instrumental instabilities and subsequent changes in signal phase and intensity during each scan. 3D diffusion-weighted images were acquired with a repetition time of 0.9 s, an echo time (TE) of 37 ms, and two signal averages (field of view 12 mm × 6 mm × 6 mm for the smallest sample (P0) and 17 mm × 11 mm × 8 mm for the largest, and others in between). The imaging matrix had dimensions from 128 × 70 × 64 to 128 × 84 × 80, which was zero-filled to double their sizes after the spectral data were apodized by a 10% trapezoidal function. The native imaging resolutions ranged from 94 μm × 86 μm × 93 μm to 133 μm × 131 μm × 100 μm. At least six diffusion weighted images with b values of 1000–1200 s/mm^2. Diffusion sensitizing gradients were applied along six different orientations: [0.707, 0.707, 0], [0.707, 0, 0.707], [0, 0.707, 0.707], [−0.707, 0.707, 0], [0.707, 0, −0.707], [0, −0.707, 0.707]. We also acquired at least one image with a b value of 150 s/mm^2. The imaging time for DTI was approximate 24 h. T_2-weighted images were acquired with the same resolution as diffusion-weighted images, with a repetition time of 0.9 s, four TE values (37 ms, 60 ms, 80 ms, 100 ms), and 2 signal averages for an additional imaging time of approximately 9 h. The total imaging time for acquiring both DT and T_2 images was approximately 33 h.

The diffusion tensor was calculated using a multivariant linear fitting method, and three pairs of eigenvalues and eigenvectors were calculated for each pixel (Basser and Pierpaoli, 1996; Basser et al., 1994). The eigenvector associated with the largest eigenvalue was referred to as the primary eigenvector. For the quantification of anisotropy, fractional anisotropy (FA) was used. Color map images were generated by combining the images of primary eigenvector and FA into RGB images. In the color map images, the ratio among R(ed), G(reen), and B(lue) components of each pixel was defined by of the ratio of the absolute values of x, y, and z components of the primary eigenvector, and the intensity was proportional to the FA. Red was assigned to the anterior–posterior axis, green to the medial-to-lateral axis, and blue to the superior–inferior axis. T_2 map images at each stage were obtained by fitting T_2-weighted images of four different TE values to a mono-exponential model. Segmentation of cortex, hippocampus, caudate putamen, cerebellum, and superior colliculus were performed manually following the definition in the Paxinos atlas (Paxinos and Franklin, 2000).

Landmark definition

We followed a coarse-to-fine hierarchical procedure to generate 3D diffeomorphic maps between mouse brain images. The first step is based on operator-identified landmarks in diffusion tensor images. Nine landmarks placed on the anterior

commissure (5 landmarks), posterior commissure (1 landmark), optic chiasm (1 landmark), and medial globus pallidus (2 landmark) enabled the initial rigid registration which roughly aligned all images to a standard position according to the standard orientation defined by the Paxinos atlas (Paxinos and Franklin, 2000).

After the initial "coarse" registration, additional landmarks were defined in aligned DTI images for better precision. Landmarks were grouped in three categories: landmarks on white matter tracts, landmarks on cortical surface, and landmarks in hippocampus. Landmarks on white matter tracts, 146 in total, were defined on DTI images (Figs. 1A and B). Of these, 82 were defined on the dorsal surface of corpus callosum and external capsule. They formed a mesh surface that approximated the boundaries between cortex and external capsule (Fig. 1C). The mesh surface was then subdivided three times using Butterfly algorithm and smoothed using Lagrange's method (Zorin et al., 1996). Starting from each of the 82 landmarks, a straight line along local surface normal intersects with the outer cortical surface, and these points of intersection were saved as cortical landmarks. The positions of these cortical landmarks were then visualized and adjusted in 3D (Fig. 1D). Landmarks in hippocampus were manually defined on 9 sagittal planes. A total 270 landmarks were defined for each mouse brain.

Large deformation diffeomorphic metric mapping (LDDMM)

The LDDMM algorithm computes a transformation $\varphi:\Omega \rightarrow \Omega$ where $\Omega \subseteq \Re^3$ is the 3D cube on which the data are defined. The computed transformation is the end point $\varphi = \varphi_1$ of a flow of velocity fields $v_t \in \boldsymbol{V}, t \in [0,1]$ given by the ordinary differential equation

$$\phi_t = v_t(\phi_t), \phi_0 = id, \tag{1}$$

where ϕ_0 the identity transformation $\phi_0(x) = x$, $\forall x \in \Omega$. As shown by Dupuis (Dupuis et al., 1998), enforcing a sufficient amount of smoothness on the elements in the space of allowable vector fields $\boldsymbol{V}$ ensures that the solution to the differential equation $\phi_t = v_t(\phi_t)$, $t \in [0,1]$ is in the space of diffeomorphisms. Throughout smoothness is enforced by defining the norm on the space $\boldsymbol{V}$ of smooth velocity vector fields through a differential operator L generally powers of the Laplacian such that $\|f\|_{\boldsymbol{V}}^2 = \|Lf\|_2^2$ where $\|\bullet\|_2$ is the standard L^2 norm for square integrable functions defined on Ω.

Throughout this work, all of the data being mapped were taken as sparse landmarks as studied in (Joshi and Miller, 2000). The mappings are therefore based on distance functions derived from sparse landmark imagery, in which an ordered collection of

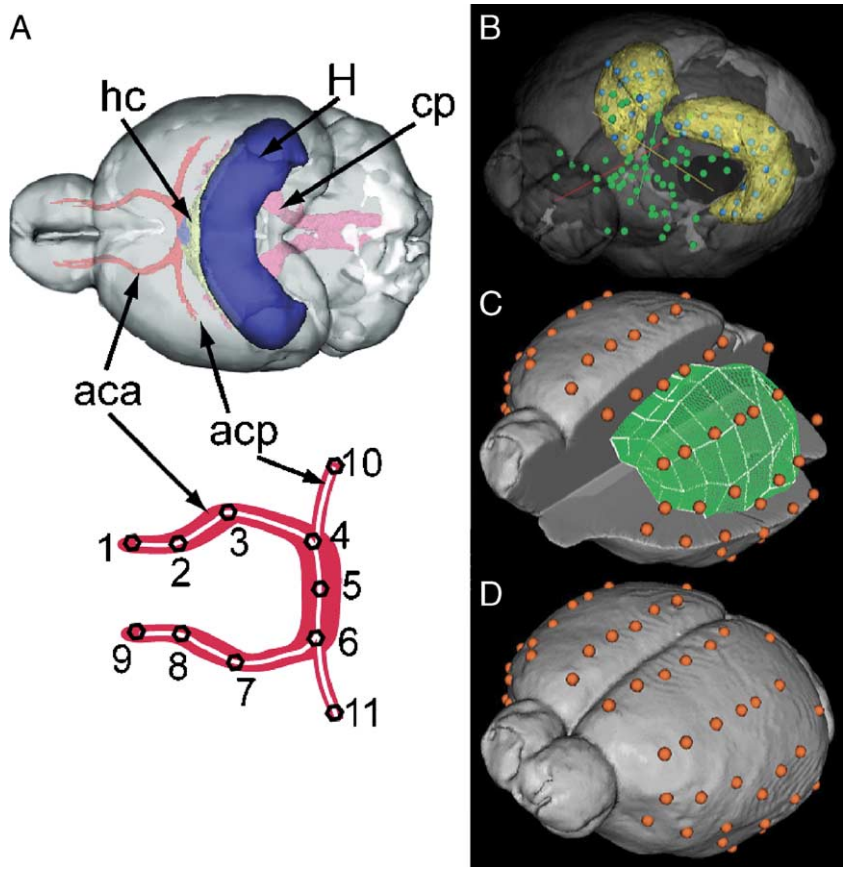

Fig. 1. Manually placed landmarks in mouse brain images and large diffeomorphic deformation metric mapping (LDDMM). Landmarks were first defined on tubular white matter tracts, for example, the anterior commissure (A). Total 60 such landmarks were defined throughout the forebrain region (visualized as green dots in B). Total 44 landmarks were defined inside hippocampus (blue dots within yellow hippocampal surfaces in panel B). Panels C and D show landmarks on cortical surfaces, and landmarks on corpus callosum, which formed a mesh surface (the green structure in panel C). Abbreviations are as follows: aca—anterior part of anterior commissure; acp—posterior part of anterior commissure; cp—cerebral peduncle; H—hippocampus; hc—hippocampal commissure.

points are defined x_k^0, x_k^1, $k = 1,\ldots,N$ with the distance function becoming

$$D_\varphi = \sum_{k=1}^{N} \left(x_k^1 - \varphi\left(x_k^0\right)\right)^t \Sigma_K \left(x_k^1 - \varphi\left(x_k^0\right)\right), \tag{2}$$

where $(\cdot)^t$ denotes matrix transpose, and Σ_k is the covariance matrix representing the error in landmark placement. The optimal φ is found as the minimum of the endpoint of the inexact matching problem

$$\inf_{\varphi = \phi_1 : \phi_1(x) = \int_0^1 v_t(\phi_t)dt + x, v \in V} \int_0^1 \|v_t\|_V^2 + \lambda D_\varphi(I, I') \tag{3}$$

Here $\lambda > 0$ is the relative weight assignment.

The Euler equation corresponding to the minimizer of Eq. (3) with the landmark distance is given by

$$v_t(x) = \sum_{k=1}^{N} K(\phi_t(x_k), x) J_{\phi_{t,1}}(\phi_t(x_k))^t \Sigma_k \left(x_k^1 - \phi_t(x_k)\right), \quad x \in \Omega, t \in [0,1] \tag{4}$$

where $J_{\phi_{t,1}} = \left(\frac{\partial \phi_{t,1}}{\partial x}\right)$ is the 3×3 Jacobian matrix of the flow from t to 1 of $\phi_{t,1}$, and where K is the 3×3 Green's kernel of V associated with the operator LL^+, L^+ the adjoint operator of L.

The algorithm for solving the Euler equation was implemented on a Pentium-4 PC with 1.7 Ghz CPU and 1 GB memory. For imaging matrix size of $272 \times 168 \times 128$ and 270 landmarks, the total computation time was 2 h. For group analysis, we performed the following analysis. Average landmark sets were obtained by averaging the landmark coordinates of all mice at each stage after rigid alignment. Using the LDDMM algorithm, we generated the following: (1) diffeomorphic maps between a landmark set and the average landmark set at P7, and (2) diffeomorphic maps between two average landmark sets at different stages. The former maps were used to study individual variations within the same stage and the latter were used to study growth. To locate brain region with significant local volume change during P7–P20 and P30–P80 period, we performed one-tailed Student's t test (IDL, Research System Inc. Boulder, CO) on the Jacobian values of diffeomorphic maps between individual mouse brain and the average P7 mouse brain.

Results

Development of mouse brains from postnatal day 0 (P0) to day 80 (P80) is shown in Fig. 2 using T_2 maps and DTI color maps in selected axial slices extracted from 3D volume data sets. T_2 maps, which are sensitive to myelin content, provided rather poor anatomical contrasts especially in pre-myelinated brains (before P30). For example, the fasciculus retroflexus (indicated by the pink arrows in Fig. 2) and the medial lemniscus (indicated by the yellow arrows in Fig. 2) can be identified in T_2 map only after P30. In comparison, DTI results provide superior and stable contrasts for delineation of various anatomical structures throughout neonatal development. White matter tracts appear as bright structures (high tissue diffusion anisotropy) with diffusion orientation tangential to the trajectories of axonal fibers. For example, the cerebral peduncle (cp) and the fasciculus retroflexus (indicated by pink arrows) appear as red structures in coronal sections (Fig. 2) as they contain axons

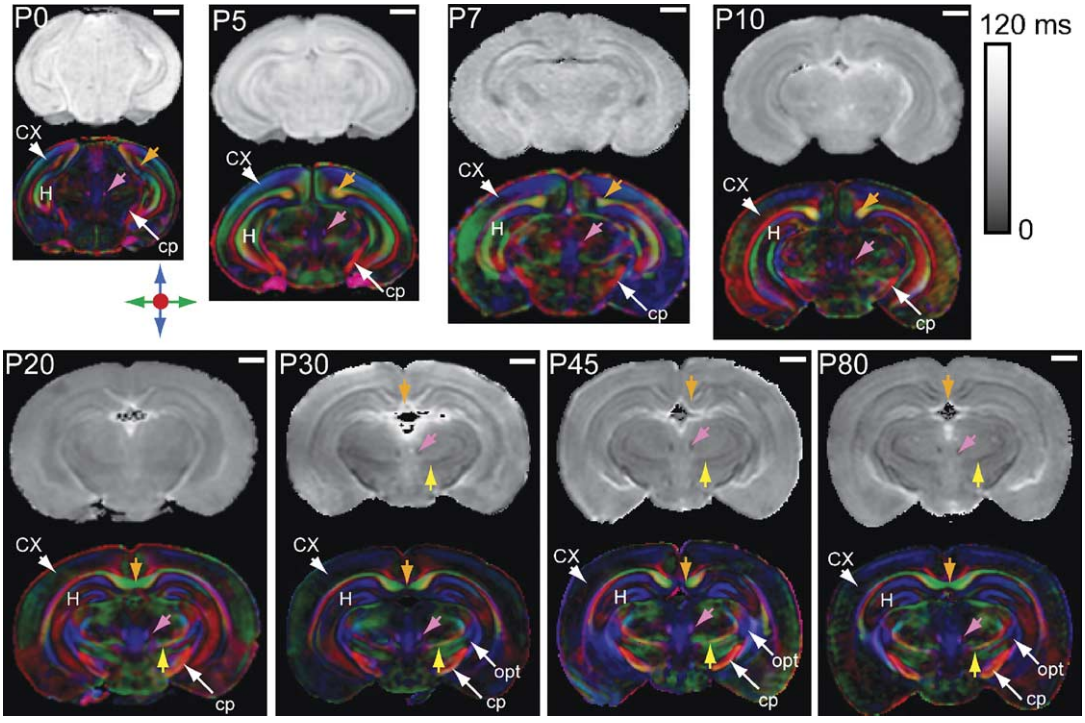

Fig. 2. T_2 and DTI color map images of postnatal mouse brains. Red indicates that local tissue orientation that is perpendicular to the plane, green indicates horizontal orientation, and blue indicates vertical orientation. All 2D images had been aligned to ensure proper orientation and position. The orange arrows indicate the locations of the forceps major of the corpus callosum during P0–P10 or the locations of splenium of the corpus callosum during P20–P80. The yellow arrows indicate the locations of medial lemniscus, and the pink arrows indicate the locations of fasciculus retroflexus. T_2 map images are scaled from 0 to 120 ms. The scale bar represents 1 mm. Structure abbreviations are as follow: CX—cortex; H—hippocampus; cp—cerebral peduncle; opt—optic tract.

running mostly in the anterior–posterior orientation. The fractional anisotropy (FA) values of white matter structures are significantly higher than those of gray matter structures at most postnatal stages. Several gray matter structures, for instance, the hippocampus, also have a relatively high anisotropy (Zhang et al., 2002). Fig. 3 demonstrates the shape changes of three major commissural fibers, the corpus callosum (orange arrows), ventral hippocampal commissure (blue arrows), and anterior commissure (red arrows) in the mid-sagittal plane. The three commissural fibers bundles appear as bright green structures in the mid-sagittal plane because they contain bundles of axons that project medio-laterally. At P2, the splenium of corpus callosum (the most posterior and thickest region of the corpus callosum) and the dorsal end of hippocampal commissure are in proximity. Starting from P5, the splenium of corpus callosum extend caudally following the growth of cortical hemisphere.

DTI enabled us to manually delineate various anatomical structures due to its excellent contrasts throughout development. The volumetric measurements of selected anatomical regions (caudate, hippocampus, and superior colliculus) are shown in Fig. 4. All structures increase their volume significantly during the first 30 days (Fig. 4B). Fig. 4C shows normalized volume ratio, in which volumes of each anatomical area are divided by the total brain volume. The results show that the rates of cortical and cerebellar growth exceed the rates of other structures during the P0–P7 (cortex) and P0–P20 (cerebellum) periods, indicating that these structures matured at relatively later stages. The non-uniform

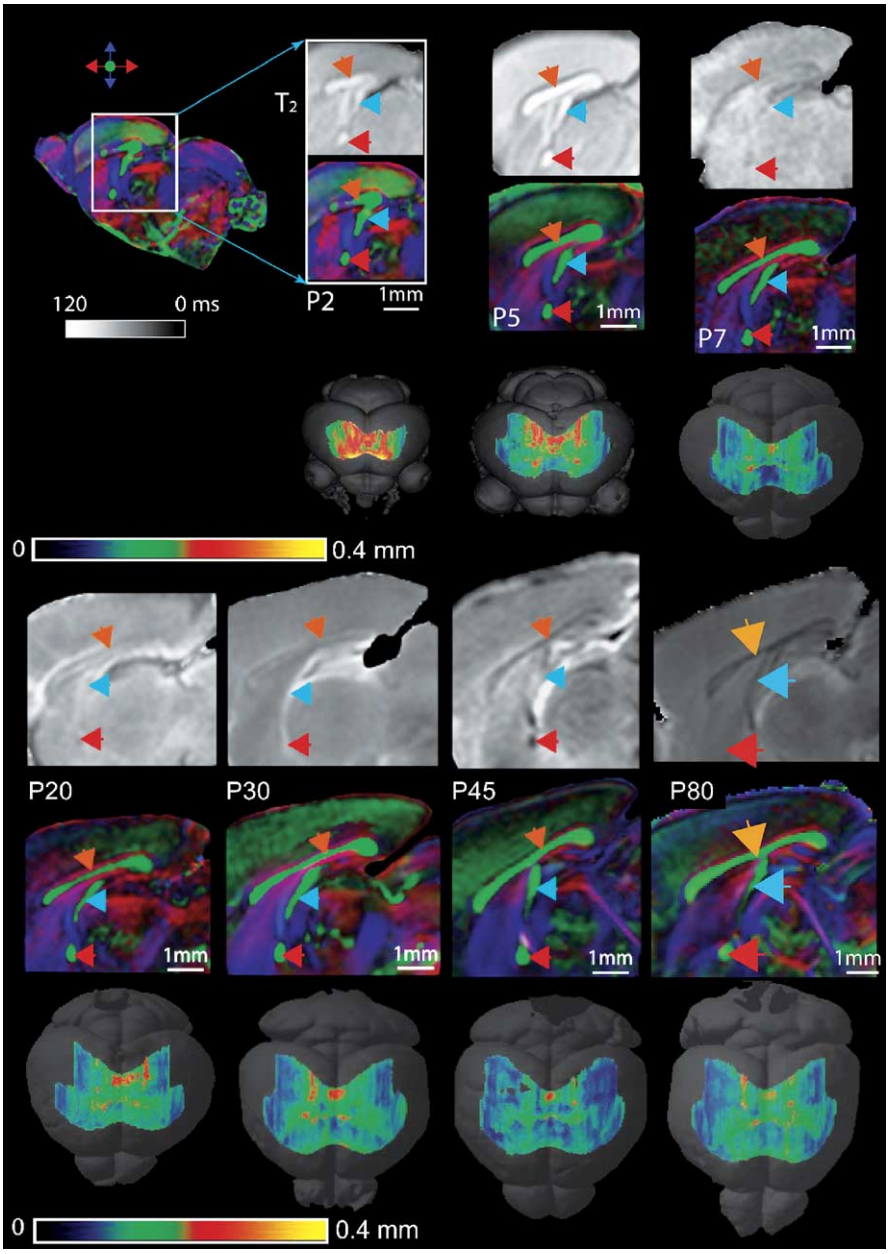

Fig. 3. DTI and T_2 map images of mid-sagittal planes of postnatal mouse brains. Corpus callosum (indicated by orange arrows), hippocampal commissure (indicated by blue arrows), and anterior commissure (indicated by red arrows) are identified in diffusion tensor (DT) images and labeled in both DT and T_2 images. Surface of corpus callosum and external capsule are color coded with local thickness.

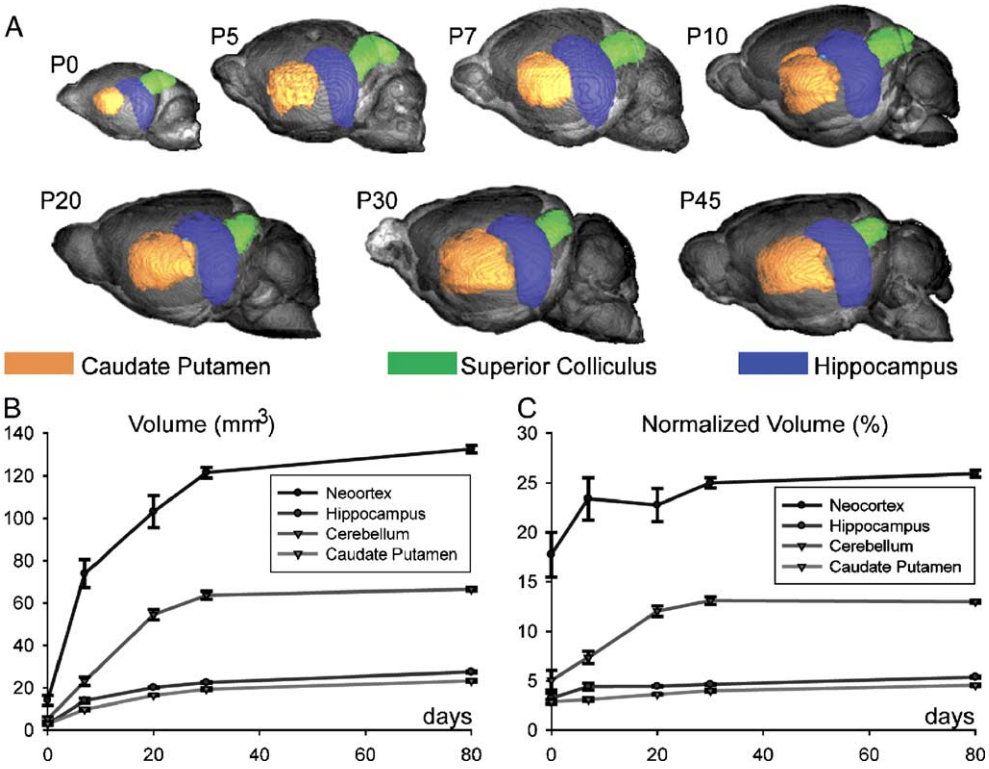

Fig. 4. Volumetric measurements with DTI. (A) Surface rendering of manually segmented caudate putamen, hippocampus, and superior colliculus in postnatal mouse brains. (B) Volumes of the neocortex, cerebellum, hippocampus, and caudate putamen during postnatal development were obtained from results of segmentation. (C) Normalized volumes of these structures (percentage of the mean whole brain volume at each stage) during postnatal development. Standard deviation of measurements are shown (n = 4).

growth rates should lead to shape changes, which can be visually appreciated in Fig. 4. For example, the cortex extends posteriorly and gradually covers the dorsal surface of the superior colliculus from P10 to P30. Comparison between MRI-based volume measurements of the brain, hippocampus, and caudate putamen and histological-based measurements of CFW and BALB mice (Fink et al., 1991) shows that the volume measurements obtained using MRI are comparable with results obtained by histologically based methods.

The relative enlargement of the cortex also causes deformation of cortico-cortical white matter tracts, most notably the corpus callosum. In a surface rendering of the corpus callosum manually segmented in the DTI results (Fig. 3), the corpus callosum extends in the lateral and posterior directions from P7 to P80, well synchronized with the growth of the cortical areas above it. Once segmented, shape parameters such as the thickness of the CC normal to the 3D surface can be readily measured and mapped on the surfaces. Interestingly, the thickness of the CC does not change, or is slightly reduced, during the period from P20 to P80, while its surface area increases drastically.

Further quantification of growth in cortical and hippocampal regions is accomplished by landmark-based large deformation diffeomorphic metric mapping (LDDMM), which measures the anatomical changes as the deviation of the inter-subject transformation from identity transformation. An example of deformation from P7 to P30 brains is shown in Fig. 5, in which a P7 brain (Fig. 5A) is deformed to a P30 brain shape (Fig. 5C). The shape of the deformed P7 brain becomes very similar to that of P30 as can be judged from the contour line of the P30 brain superimposed on the deformed P7 brain (Fig. 5B).

To visualize the LDDMM results, we used a vector map (Fig. 5D) and a Jacobian map (Fig. 5E). In vector maps, a vector shows voxel displacement due to deformation, with both the length and color of the vector reflects the magnitude of local displacement. A Jacobian map (the determinant of the gradient of the diffeomorphic map) shows local volumetric changes, with values greater than unity corresponds to volume growth, values smaller than unity for volume loss and unity for no volume change. In Fig. 5E, a uniform grid representing voxels in the template images is deformed and overlaid with color-coded local Jacobian values to illustrate the local deformation (see the enlarge image Fig. 5G). The results suggest that growth between P7 and P30 is mostly concentrated in the cortex, confirming the manual-based segmentation and volume measurement results (Fig. 4). This analysis further locates areas of active growth within the cortex and the direction of tissue movements. For example, at this coronal level, two lateral regions of cerebral cortex showed the most significant growth.

To estimate the sensitivity of our techniques to errors in landmark placement, random perturbations at different levels were added to manually defined landmark sets. We tried four increasing noise levels and ran six simulations at each level. A normal distribution of random noise (σ = 1.0 pixel) can cause an averaged displacement of 1.561 (±0.724) pixel to each landmark, with a maximum displacement of 4 pixels. We computed diffeomorphic transformations using both perturbed landmark sets and the original landmark set, and applied these maps to triangulated cortical surface consisted of 56,884 triangles and 28,404 vertexes. We examined the differences between different deformed surfaces by averaged distance between corresponding vertexes (Fig. 6B)

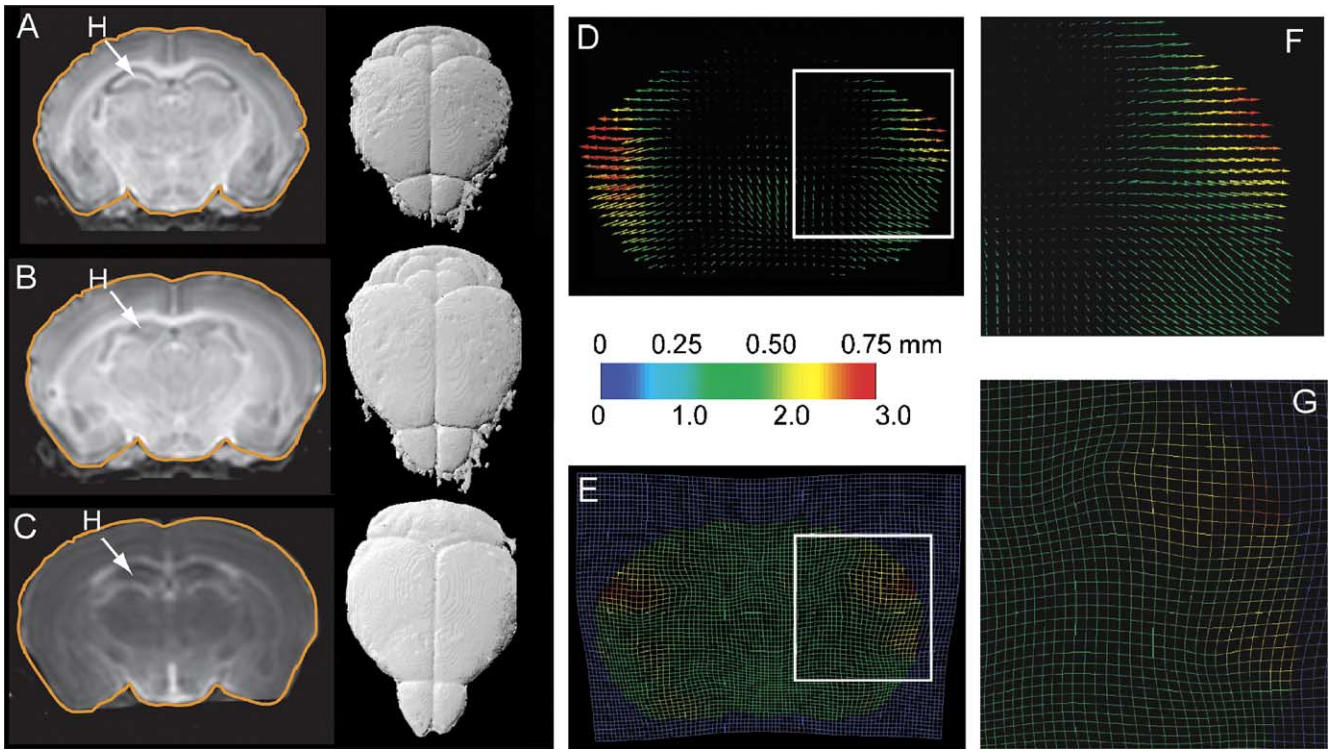

Fig. 5. Large deformation landmark matching of a P7 mouse brain image to a P30 images. (A and C) Coronal MR images of the P7 mouse brain (A) and the P30 mouse brain (C) are shown with brain boundaries marked by orange curves. (B) Deformed P7 brain image is overlaid with the boundary of the P30 brain. The 3D brain surfaces are rendered next to the 2D images for the P7, deformed P7, and P30 mouse brains. The diffeomorphic map is visualized as color-coded vector map (D) and Jacobian map (E) with enlarged local areas shown in panels F and G, respectively.

and differences of surface areas (Fig. 6C). The distance between corresponding vertexes is below 1 pixel after perturbations with a standard deviation of 1 pixel are applied, and the same amount of perturbation caused 1% error in surface area results. These results suggest that small error in landmark placement can be permitted for successful landmark matching.

Fig. 7 shows the spatial pattern of local tissue volume change and its statistical significance in P7–P20 and P30–P80 periods.

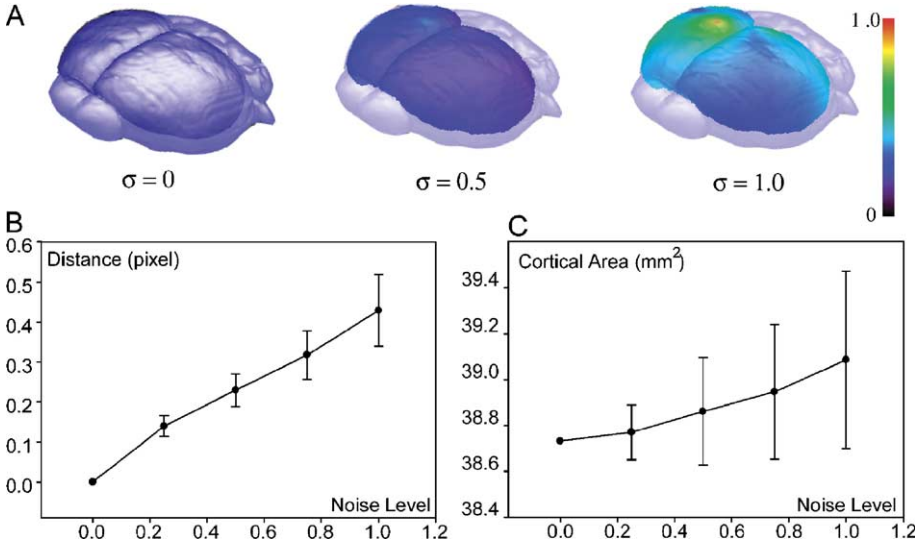

Fig. 6. Sensitivity of our landmark matching techniques to the errors in landmark placement. Diffeomorphic maps were computed using landmarks with random noises (perturbation) at four different levels ($n = 6$ for each level) added to the landmarks. The maps were then used to deform the cortical surface of a P45 mouse brain. Panel A shows how deformed cortical surfaces with two different levels of perturbation (Gaussian distributed zero mean with $\sigma = 0.5$ or $\sigma = 1.0$) compared with no perturbation to landmarks ($\sigma = 0$). The distances between the original surface and deformed surfaces were color coded and mapped on the original surface. Panel B shows the averaged distances between the original surface and perturbed surfaces with different perturbations, and panel C shows cortical areas with different levels of perturbations.

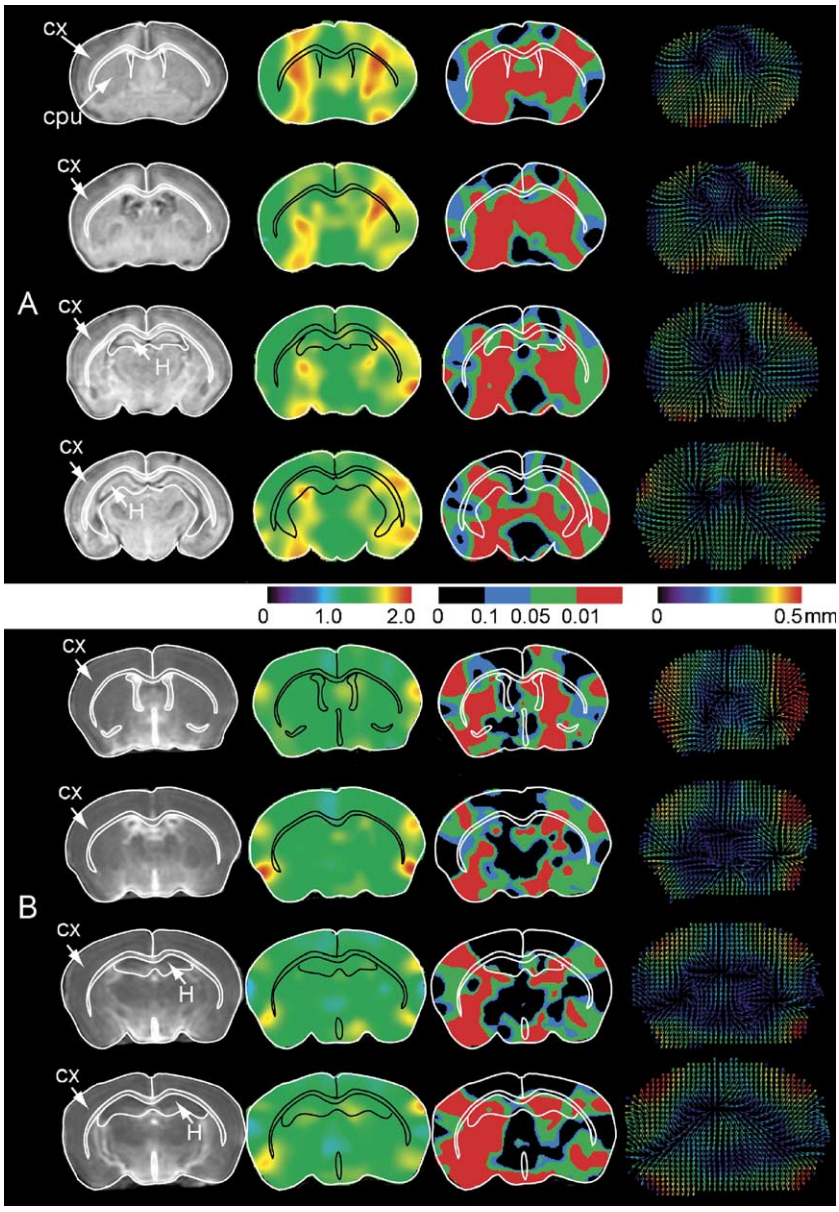

Fig. 7. Volumetric growth, its statistical significance, and tissue displacement in developing mouse brains between P7 and P20 (A) and between P30 and P80 (B). The left most column shows three coronal sections of the average P7 mouse brain (A) and the average P30 mouse brain (B). The brain, corpus callosum, and hippocampus are outlined. The second column shows the Jacobian maps between P7 and P20 (A) and between P30 and P80 (B) that visualize the volume changes between the average mouse brains. A value of unity (light blue) indicates no volume change. A value of 2 (red) indicates the local tissue volume doubles. The third column displays the statistical significance derived from one-tailed Student's *t* test. Red regions have a *P* value of less than 0.01, green regions have a *P* value between 0.01 and 0.05, and blue regions have a *P* value between 0.05 and 0.1. The right most column shows the tissue displacement. Abbreviations are as follows: CPU—caudate putamen; CX—neocortex; H—hippocampus.

The Jacobian map (Fig. 7A, the second column from the left) between the average P7 and the average P20 mouse brains reveals that volumes of most brain regions increase (green to red), with large increase occurs in the cortex, caudate putamen, and hippocampus. In comparison, volume growth during the P30–P80 period (Fig. 7B, the second column from the left) is smaller in terms of volume increase with several regions showing no apparent volume change (light blue). Statistical analysis (Fig. 7, the third column from the left) suggests that the growth delineated in the Jacobian maps at P7–P20 period is highly significant (most regions with $P < 0.05$). In the displacement maps (Fig. 7, the right column), both the P7–P20 period and the P30–P80 period show large tissue displacement of approximately 0.5 mm with directions mostly pointing in radial orientations with respect to the brain surface.

Discussion

In this paper, we describe DTI-based macroscopic and quantitative measurements of mouse brain development, which is expected to enhance our ability for morphological characterization.

Previous studies demonstrated that DTI provides excellent image contrast to delineate prenatal mouse brains (Mori et al., 2001; Zhang et al., 2003). We show that DTI is a valuable tool for studying mouse brain development during the early postnatal phase (P0–P30). Conventional MRI based on tissue relaxation parameters often has rather poor contrasts for the characterization of premyelinated brain anatomy (Fig. 2). Studies have shown that contrasts can be enhanced with the addition of MR-detectable contrast agents, such as MR neuronal tract-tracing using manganese (Mn^{2+}) (London et al., 1989; Pautler et al., 1998; Saleem et al., 2002). While the Mn^{2+}-based approach has advantages in identifying specific white matter tracts related to Mn^{2+} administration sites and observing its modulation due to functional status of the host (Lin and Koretsky, 1997), it may not be suitable for monitoring the anatomy of the entire brain. For example, injection of manganese chloride ($MnCl_2$) in the eye reveals visual pathways but not other pathways in the brain. In comparison, DTI provides distinctive endogenous contrast for whole brain tissue delineation and the contrast pattern is consistent during the entire course of postnatal development (Figs. 2, 3). In this regard, DTI is well suited for the characterization of developing brain phenotypes.

With the superb contrast provided by DTI, many brain regions can be detected manually based on DTI images throughout brain development, which provides volumetric measurement of major brain compartments during development (Fig. 4). Volume measurement is an effective and widely used index for morphological analysis. These results show a similar trend in cortical development as reported by previous studies using rat (Uylings et al., 1990) and are comparable to results from other mouse strains (Fink et al., 1991). Geometrical information can also be obtained from the segmented data as demonstrated in Fig. 3, in which the thickness of the corpus callosum is mapped at each stage.

It is a challenging task to visualize and comprehend the evolution of mouse brain anatomy during development. Tissue growth is not necessarily spatially uniform across the brain, and different brain regions may possess different spatial–temporal growth characteristics. Direct inspection of 2D images (Figs. 2 and 3) cannot be used for analyzing shape changes because the structures may stay in the same section or move to different section between two developmental stages. This difficulty can be solved with DTI coupled with techniques of computational anatomy. DTI provides the consistent contrast throughout development process, which is necessary to follow the growth of various tissue compartments, and computational techniques take the DTI results as inputs to localize developmental changes. In this study, we adopted landmark-based LDDMM techniques, which quantify shape differences based on a set of points that indicate corresponding anatomical locations between two brains (Fig. 5). We assessed the effect of non-reproducible landmark placement by processing the same data set multiple times with variable placement errors, which showed the robustness of this approach against small errors. Fig. 7 shows the spatial patterns of brain development measured by the landmark matching. To our knowledge, this is the first demonstration of 3D quantitative description of deformation mapping of the developing mouse brain structures.

In this study, we used a landmark-based approach for measuring anatomical changes instead of direct image matching (Ashburner et al., 2003; Christensen et al., 1996; Shen and Davatzikos, 2003; Thompson and Toga, 1996; Thompson et al., 1996) because direct vector or tensor image matching technique that utilizes the complex information provided by DTI is presently not available.

It is necessary to note the limitations of our approach. First, DTI has inherently low signal-to-noise, which leads to lower spatial resolution and/or longer scanning time compared to conventional MRI. In this paper, we achieved approximately 100 μm isotropic resolution with 24 h of imaging time. Employment of faster imaging techniques will be an important future research effort. Second, landmark placement is time consuming and susceptible for human errors. To accurately capture developmental changes, a dense network of landmarks is required. For future studies with large population of animals, landmark-based techniques may not be the optimal solution. Development of direct tensor field matching will greatly enhance the efficiency of the study. The results in this report are sensitive not only to growth between different stages but also to individual variations and experimental errors such as shrinkage and deformation during the fixation and storage processes. Currently our DTI database has only a limited amount of data at each developmental stage, examination of a large number of animals will be an important research effort in the future.

In conclusion, DTI has a clear advantage over conventional MRI for the delineation of mouse brain structures during postnatal development. The rich anatomical details revealed by DTI were used as neuroanatomical landmarks in tracing anatomical changes using LDDMM. Using this approach, we have characterized the spatial and temporal growth patterns of forebrain structures.

Acknowledgments

This study was supported by NIH grants RO1 AG20012-01, RO3 HD41407-01A1, and P41 RR15241-01.

References

Alvarez-Bolado, G., Swanson, W.L., 1996. Developmental Brain Maps: Structure of the Embryonic Rat Brain. Elsevier, New York.

Ashburner, J., Csernansky, G.J. et al., 2003. Computer-assisted imaging to assess brain structure in healthy and diseased brains. Lancet Neurol., 2 (2), 79–88.

Baratti, C., Barnett, S.A. et al., 1999. Comparative MR imaging study of brain maturation in kittens with T1, T2, and the trace of the diffusion tensor. Radiology, 210 (1), 133–142.

Basser, P., Pierpaoli, C., 1996. Microstructural and physiological features of tissues elucidated by quantitative-diffusion-tensor MRI. J. Magn. Reson., Ser. B, 111, 209–219.

Basser, P.J., Mattiello, J. et al., 1994. Estimation of the effective self-diffusion tensor from the NMR spin echo. J. Magn. Reson., Ser. B, 103 (3), 247–254.

Bayer, S., Altman, J., 1991. Neocortical Development. Raven Press.

Bayer, S.A., Zhang, X. et al., 1994. Three-dimensional reconstructions of the developing forebrain in rat embryos. NeuroImage, 1 (4), 296–307.

Beg, M.F., Miller, M. et al., 2003. The Euler–Lagrange equation for interpolating sequence of landmark datasets. Medical Image Computing and Computer-Assisted Intervention-Miccai, Pt. 2, vol. 2879, pp. 918–925.

Bookstein, F.L., 1996. Biometrics, biomathematics and the morphometric synthesis. Bull. Math. Biol., 58 (2), 313–365.

Christensen, G.E., Rabbit, D.R. et al., 1996. Deformable templates using large deformation kinematics. IEEE Trans. Image Process., 5 (10), 1435–1447.

Chung, M.K., Worsley, J.K. et al., 2001. A unified statistical approach to deformation-based morphometry. NeuroImage, 14 (3), 595–606.

Dann, R., Hoford, J. et al., 1989. Evaluation of elastic matching system for anatomic (Ct, Mr) and functional (Pet) cerebral images. J. Comput. Assist. Tomogr., 13 (4), 603–611.

Dupuis, P., Grenander, U. et al., 1998. Variational problems on flows of diffeomorphisms for image matching. Q. Appl. Math., 56 (3), 587–600.

Evans, A.C., Collins, L.D. et al., 1996. Computational approaches to quantifying human neuroanatomical variability. Brain Mapping: The Methods. Academic Press, New York, pp. 343–361.

Fink, G.R., Zilles, K. et al., 1991. Postnatal development of forebrain regions in the autoimmune NZB-mouse. A model for degeneration in neuronal systems. Anat. Embryol. (Berl.), 183 (6), 579–588.

Good, C.D., Johnsrude, S.I. et al., 2001. A voxel-based morphometric study of ageing in 465 normal adult human brains. NeuroImage, 14 (1), 21–36.

Grenander, U., Miller, I.M., 1998. Computational anatomy: an emerging discipline. Q. Appl. Math., LVI (4), 617–694.

Jacobs, R.E., Fraser, E.S., 1994. Imaging neuronal development with magnetic resonance imaging (NMR) microscopy. J. Neurosci. Methods, 54 (2), 189–196.

Jacobs, R.E., Ahrens, T.E. et al., 1999. Towards a microMRI atlas of mouse development. Comput. Med. Imaging Graph., 23 (1), 15–24.

Jacobs, R.E., Ahrens, T.E. et al., 1999. Looking deeper into vertebrate development. Trends Cell Biol., 9 (2), 73–76.

Johnson, G.A., Benveniste, H. et al., 1993. Histology by magnetic resonance microscopy. Magn. Reson. Q., 9 (1), 1–30.

Johnson, G.A., Cofer, P.G. et al., 2002. Morphologic phenotyping with MR microscopy: the visible mouse. Radiology, 222 (3), 789–793.

Joshi, S., Miller, M., 2000. Landmark matching via large deformation diffeomorphism. IEEE Trans. Image Process., 9 (8), 1357–1370.

Lin, Y.J., Koretsky, P.A., 1997. Manganese ion enhances T1-weighted MRI during brain activation: an approach to direct imaging of brain function. Magn. Reson. Med., 38 (3), 378–388.

London, R.E., Toney, G. et al., 1989. Magnetic resonance imaging studies of the brains of anesthetized rats treated with manganese chloride. Brain Res. Bull., 23 (3), 229–235.

Miller, M.I., Younes, L., 2001. Group actions, homeomorphisms, and matching: a general framework. Int. J. Comput. Vis., 41 (1/2), 61–84.

Miller, M., Banerjee, A. et al., 1997. Statistical methods in computational anatomy. Stat. Methods Med. Res., 6 (3), 267–299.

Miller, M., Trouve, A. et al., 2002. On the metrics and Euler–Lagrange equations of computational anatomy. Annu. Rev. Biomed. Eng., 4, 375–405.

Mori, S., van Zijl, P.C., 1998. A motion correction scheme by twin-echo navigation for diffusion-weighted magnetic resonance imaging with multiple RF echo acquisition. Magn. Reson. Med., 40 (4), 511–516.

Mori, S., Itoh, R. et al., 2001. Diffusion tensor imaging of the developing mouse brain. Magn. Reson. Med., 46 (1), 18–23.

Pautler, R.G., Silva, C.A. et al., 1998. In vivo neuronal tract tracing using manganese-enhanced magnetic resonance imaging. Magn. Reson. Med., 40 (5), 740–748.

Paxinos, G., Franklin, K., 2000. The Mouse Brain in Stereotaxic Coordinates. Academic Press, San Diego, CA.

Paxinos, G., Ashwell, K. et al., 1994. Atlas of the Developing Rat Nervous System. Academic Press, San Diego, CA.

Saleem, K.S., Pauls, M.J. et al., 2002. Magnetic resonance imaging of neuronal connections in the macaque monkey. Neuron, 34 (5), 685–700.

Sharpe, J., Ahlgren, U. et al., 2002. Optical projection tomography as a tool for 3D microscopy and gene expression studies. Science, 296 (5567), 541–545.

Shen, D., Davatzikos, C., 2003. Very high-resolution morphometry using mass-preserving deformations and HAMMER elastic registration. NeuroImage, 18 (1), 28–41.

Thompson, P., Toga, W.A., 1996. A surface-based technique for warping three-dimensional images of the brain. IEEE Trans. Med. Imaging, 15 (4), 402–417.

Thompson, P.M., Schwartz, C. et al., 1996. High-resolution random mesh algorithms for creating a probabilistic 3D surface atlas of the human brain. NeuroImage, 3 (1), 19–34.

Thompson, P.M., Giedd, N.J. et al., 2000. Growth patterns in the developing brain detected by using continuum mechanical tensor maps. Nature, 404 (6774), 190–193.

Thompson, P.M., Cannon, D.T. et al., 2001. Genetic influences on brain structure. Nat. Neurosci., 4 (12), 1253–1258.

Thompson, P.M., Vidal, C. et al., 2001. Mapping adolescent brain change reveals dynamic wave of accelerated gray matter loss in very early-onset schizophrenia. Proc. Natl. Acad. Sci. U. S. A., 98 (20), 11650–11655.

Thompson, P.M., Hayashi, M.K. et al., 2003. Dynamics of gray matter loss in Alzheimer's disease. J. Neurosci., 23 (3), 994–1005.

Toga, A.W., Thompson, M.P., 2003. Temporal dynamics of brain anatomy. Annu. Rev. Biomed. Eng., 5, 119–145.

Uylings, H., Van Eden, C. et al., 1990. The prenatal and postnatal development of rat cerebral cortex. In: Kolb, B., Tees, R. (Eds.), The Cerebral Cortex of the Rat. MIT Press, Boston, MA, pp. 35–76.

van Pelt, J., van Ooyen, A. et al., 2001. The need for integrating neuronal morphology databases and computational environments in exploring neuronal structure and function. Anat. Embryol. (Berl.), 204 (4), 255–265.

Weninger, W.J., Mohun, T., 2002. Phenotyping transgenic embryos: a rapid 3-D screening method based on episcopic fluorescence image capturing. Nat. Genet., 30 (1), 59–65.

Zhang, J., van Zijl, P.C. et al., 2002. Three-dimensional diffusion tensor magnetic resonance microimaging of adult mouse brain and hippocampus. NeuroImage, 15 (4), 892–901.

Zhang, J., Richards, J.L. et al., 2003. Three-dimensional anatomical characterization of the developing mouse brain by diffusion tensor microimaging. NeuroImage, 20 (3), 1639–1648.

Zorin, D., Schroder, P. et al., 1996. Interpolating Subdivisions for Meshes with Arbitrary Topology. ACM SIGGRAPH.